Supplementary Information

for

Universality of the 1/9 Magnetization Plateau and Quantum-Disordered States in the Kagome Family $Cs_8AB_3Ti_{12}F_{48}$ (A = Rb, Li; B = K, Na)

Prena Chaudhary[1], Asiri Thennakoon[1], Tommy Park[1], Hanru Wang[2], Leshan Zhao[3], Laurel Winter[4], Neil Herrison[4], Christina Hoffmann[5], Junghong H. He[5], Harald O. Jeschke[6], H. Nojiri[7], Akira Matsuo[8], Koichi Kindo[8], Takahashi Miwako[9], Yukio Noda[8,10], Taku J. Sato[8,10,11], Shiyan Li[2], Hiroaki Ueda[12], Gia-Wei Chern[1], and Seung-Hun Lee[1]

[1]Department of Physics, University of Virginia; Charlottesville, Virginia, 22904, USA.

[2]State Key Laboratory of Surface Physics, Department of Physics, Fudan University, Shanghai 200438, China

[3]Institute for Quantum Matter and Department of Physics and Astronomy, The Johns Hopkins University; Baltimore, Maryland, 21218, USA.

[4]National High Magnetic Field Laboratory, Los Alamos National Laboratory, Los Alamos, NM, 87545, USA

[5]Oak Ridge National Laboratory, Oak Ridge, Tennessee, 37831, USA.

[6]Research Institute for Interdisciplinary Science, Okayama University, Okayama 700-8530, Japan

[7]Institute for Materials Research, Tohoku University, Sendai 980-8577, Japan

[8]Institute for Solid State Physics, University of Tokyo, Kashiwa, 277-8581, Japan

[9]Department of Materials Science, Institute of Pure and Applied Sciences, University of Tsukuba, Ibaraki, Tsukuba, 305-8573, Japan

[10]Institute of Multidisciplinary Research for Advanced Materials, Tohoku University, Sendai 980-8577, Japan

[11]Trans-scale Quantum Science Institute, University of Tokyo, Tokyo 113-0033, Japan

[12]Co-Creation Institute for Advanced Materials, Shimane University, 1060 Nishikawatsu-cho, Matsue, Shimane 690-8504 Japan

SUPPLEMENTARY NOTE 1: Magnetic susceptibility and Curie-Weiss analysis of the $Cs_8AB_3Ti_{12}F_{48}$ family.

The temperature-dependent magnetic susceptibilities of $Cs_8LiNa_3Ti_{12}F_{48}$, $Cs_8LiK_3Ti_{12}F_{48}$, and $Cs_8RbK_3Ti_{12}F_{48}$ exhibit broad behavior characteristic of antiferromagnetically correlated systems. To estimate the dominant magnetic interaction scale, the inverse susceptibility, $1/\chi(T)$, was fitted to the Curie-Weiss relation over 150-300 K, where short-range correlation effects are reduced. The fits yield Curie-Weiss temperatures of $\theta_{CW} = -36.9$ K for LiNa, $\theta_{CW} = -40.4$ K for LiK, and $\theta_{CW} = -47.4$ K for RbK. The negative Curie-Weiss temperatures indicate dominant antiferromagnetic interactions in all three compounds.

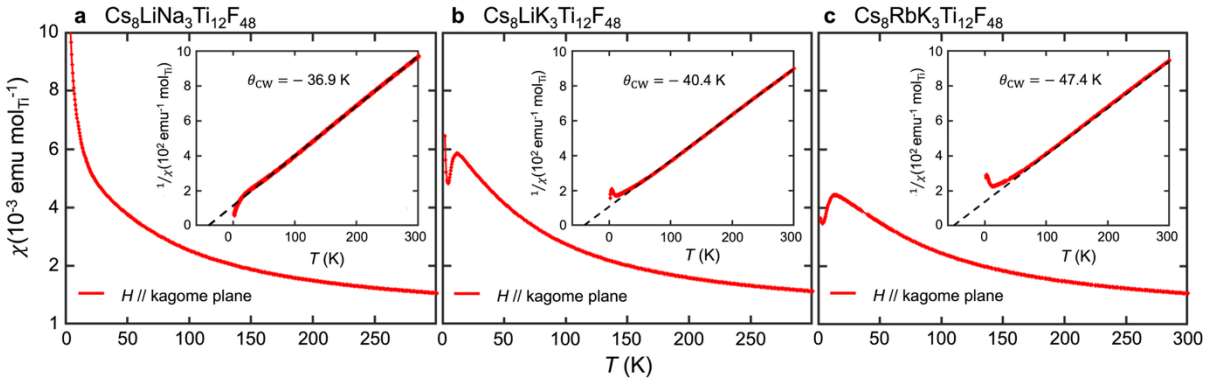

Supplementary Fig. 1 | Temperature-dependent magnetic susceptibility and Curie–Weiss analysis of the $Cs_8AB_3Ti_{12}F_{48}$ family. Single-crystal magnetic susceptibility $\chi(T)$ measured from approximately 2 to 300 K under an applied magnetic field of H = 1 T parallel to the kagome plane for **a,** $Cs_8LiNa_3Ti_{12}F_{48}$; **b,** $Cs_8LiK_3Ti_{12}F_{48}$; and **c,** $Cs_8RbK_3Ti_{12}F_{48}$. Insets show the corresponding inverse susceptibilities, $1/\chi(T)$, and Curie–Weiss fits over 150–300 K.

SUPPLEMENTARY NOTE 2: Electron Spin Resonance (ESR) measurements

Experimental procedure

High-field electron spin resonance (ESR) measurements were performed in transmission geometry on single crystals of LiNa, RbK, and LiK at the Institute for Materials Research, Tohoku University. Measurements were conducted using the high-field THz-ESR (TESLA-ESR) system equipped with a ^{3}He low-temperature cryostat and pulsed magnetic fields generated by capacitor discharge. Each crystal was mounted separately, with the microwave frequency and temperature varied between runs. The measurements relevant to the present analysis covered the frequency range 135-405 GHz. The frequency-field data used to determine the effective g factors were collected at 0.5 K with the magnetic field applied perpendicular to the kagome plane ($H \perp$ kagome plane). The RbK spectrum measured at 135 GHz was excluded from the quantitative analysis because the resonance feature was strongly affected by noise and background contributions.

ESR spectra and resonance-field determination

Representative frequency-dependent ESR spectra measured at 0.5 K are shown in Supplementary Fig. 2. For visualization, the displayed spectra were linearly background-subtracted, smoothed using a five-point moving average, normalized to the resonance-dip amplitude, and vertically offset. These processing steps were applied only for presentation; all resonance-field fits were performed on the unprocessed raw data using the SciPy Python library.

The ESR spectra exhibit broad absorption minima spanning several tesla, which shift systematically toward higher magnetic fields with increasing microwave frequency. This behavior is clear resolved at lower frequencies but becomes less distinct at higher frequencies as the signal-to-noise ratio decreases. For each frequency, the resonance field, B_0, was defined as the center of the dominant absorption minimum obtained from a Lorentzian or Gaussian line-shape fit, as appropriate for the observed profile. The analysis assumed a single dominant broad absorption feature within the selected field window.

The measurement system recorded one magnetic-field-monitor channel (CH1) and three same-frequency microwave-transmission channels. Only the rising-field portion of the pulsed-field trace was used for the resonance-field analysis. The magnetic field was obtained from $B = f_{\mathrm{cal}} \times \mathrm{CH1}$, where $f_{\mathrm{cal}} = 0.881$ T V^{-1} is the field-calibration factor.

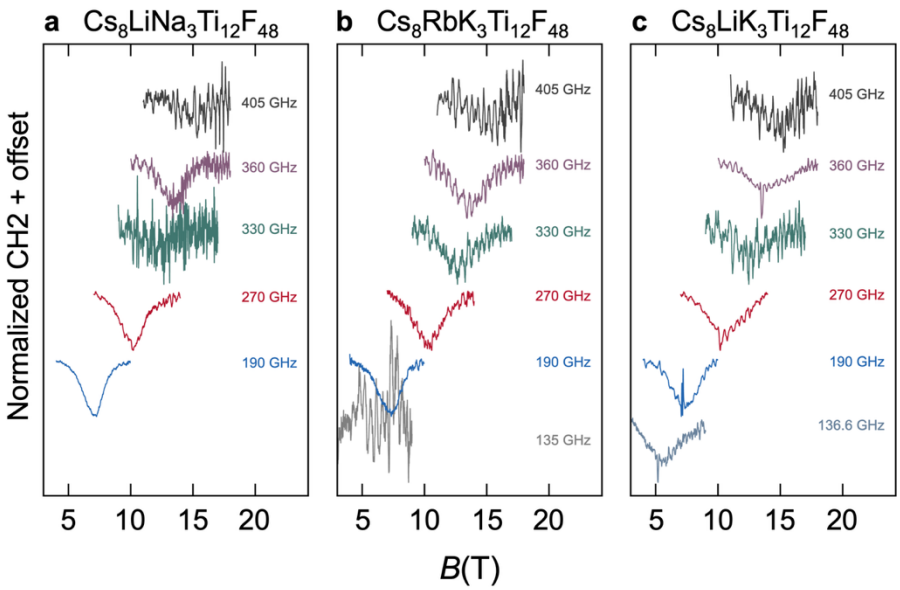

Supplementary Fig. 2 | Frequency-dependent high-field ESR spectra measured at 0.5 K. a, $Cs_8LiNa_3Ti_{12}F_{48}$; **b,** $Cs_8RbK_3Ti_{12}F_{48}$; and **c,** $Cs_8LiK_3Ti_{12}F_{48}$. Normalized rise-field CH2 transmission spectra are plotted as a function of magnetic field and vertically offset for clarity. The microwave frequency is indicated next to each trace. The spectra shown here were processed only for visualization, whereas the resonance fields used in the quantitative analysis were obtained by fitting the unprocessed raw data. The gray RbK spectrum measured at 135 GHz was excluded from the frequency-field analysis because the resonance feature was obscured by a low signal-to-noise ratio and substantial background contribution.

Determination of the effective g factor

The resonance frequencies were plotted as a function of the corresponding resonance field, as shown in Supplementary Fig. 3. For an ESR transition dominated by Zeeman splitting, the resonance frequency and magnetic field are related by $h\nu = g_{\mathrm{eff}}\mu_{\mathrm{B}}B_0$, where h is Planck's constant, ν is the microwave frequency, g_{eff} is the effective spectroscopic g factor, and μ_{B} is the Bohr magneton. To allow for a possible small offset, the measured frequency-field dependence was fitted using $\nu = mB_0 + c$, and the effective g factor was calculated from $g_{\mathrm{eff}} = \frac{m}{\mu_{\mathrm{B}}/h} = \frac{m}{13.996245\ \mathrm{GHz\ T^{-1}}}$, where $\mu_{\mathrm{B}}/h = 13.996245\ \mathrm{GHz\ T^{-1}}$ and m is the fitted slope.

The accepted resonance points show an approximately linear frequency-field dependence (supplementary Fig. 3), yielding $g_{\mathrm{eff}} = 1.940(30)$ for LiNa, $g_{\mathrm{eff}} = 1.915(33)$ for RbK, and $g_{\mathrm{eff}} = 1.975(70)$ for LiK. The resonance-center uncertainties were propagated into the weighted regression. The quoted uncertainties are the standard errors of the fitted slopes and do not include systematic uncertainty in the magnetic field at the sample.

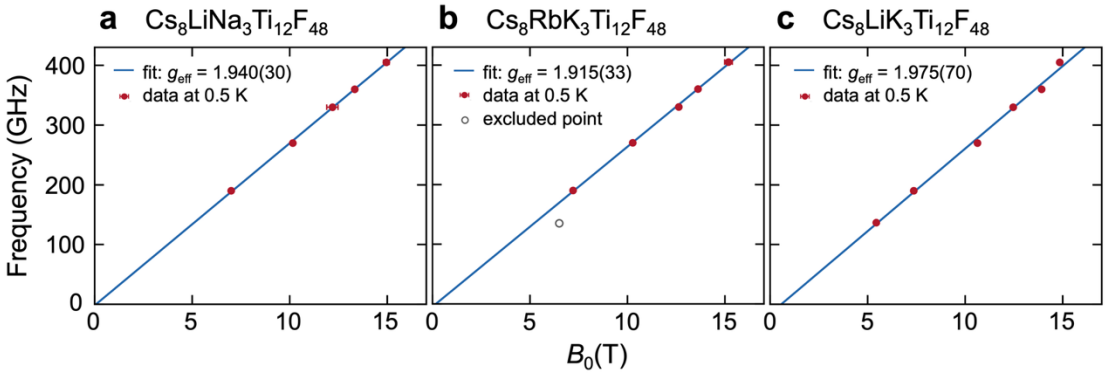

Supplementary Fig. 3 | Frequency-field dispersion at 0.5 K. a, $Cs_8LiNa_3Ti_{12}F_{48}$; **b,** $Cs_8RbK_3Ti_{12}F_{48}$; and **c,** $Cs_8LiK_3Ti_{12}F_{48}$. Filled red symbols show the resonance fields included in the analysis, and solid lines represent linear fits of $\nu = mB_0 + c$, with the intercept allowed to vary. The open symbol for RbK at 135 GHz was excluded because of its low signal-to-noise ratio and background contributions. Horizontal error bars show the fitted uncertainties in B_0.

Estimated field range of the 1/9 magnetization plateau

To relate the ESR-derived g factors to the high-field magnetization measurements, the theoretical field interval associated with the 1/9 magnetization plateau, $0.35 < g\mu_B H/J < 0.42$, was converted into magnetic field units. For each boundary of this interval, $x = 0.35$ and 0.42, the corresponding magnetic field is $H = x\left(\frac{k_B}{\mu_B}\right)\frac{J/k_B}{g_{\text{eff}}}$. The characteristic exchange scale was estimated from the magnitude of the Curie-Weiss temperature, using $J/k_B \approx |\theta_{\text{CW}}|$. Using $|\theta_{\text{CW}}| = 47.4$ K for RbK and 40.4 K for LiK gives the field ranges summarized in Supplementary Table 1. LiNa is not included in this comparison because no clear 1/9 magnetization plateau-like feature is observed in its high-field magnetization.

Supplementary Table 1 | Theoretical 1/9 plateau field ranges calculated using the ESR-derived effective g values at 0.5 K. The field ranges were obtained from the theoretical dimensionless interval $0.35 < g\mu_B H/J < 0.42$ using $J/k_B \approx |\theta_{\text{CW}}|$ as an estimate of the characteristic exchange scale. The central values of the ESR-derived g_{eff} factors were used to calculate the lower and upper field boundaries.

Compound	g_{eff} at 0.5 K	J/k_B(K)	Estimated 1/9 plateau frange (T)
RbK	1.915(33)	47.4	12.9 – 15.5
LiK	1.975(70)	40.4	10.7 – 12.8

SUPPLEMENTARY NOTE 3: Temperature dependence of highfield magnetization for fields perpendicular to the kagome plane.

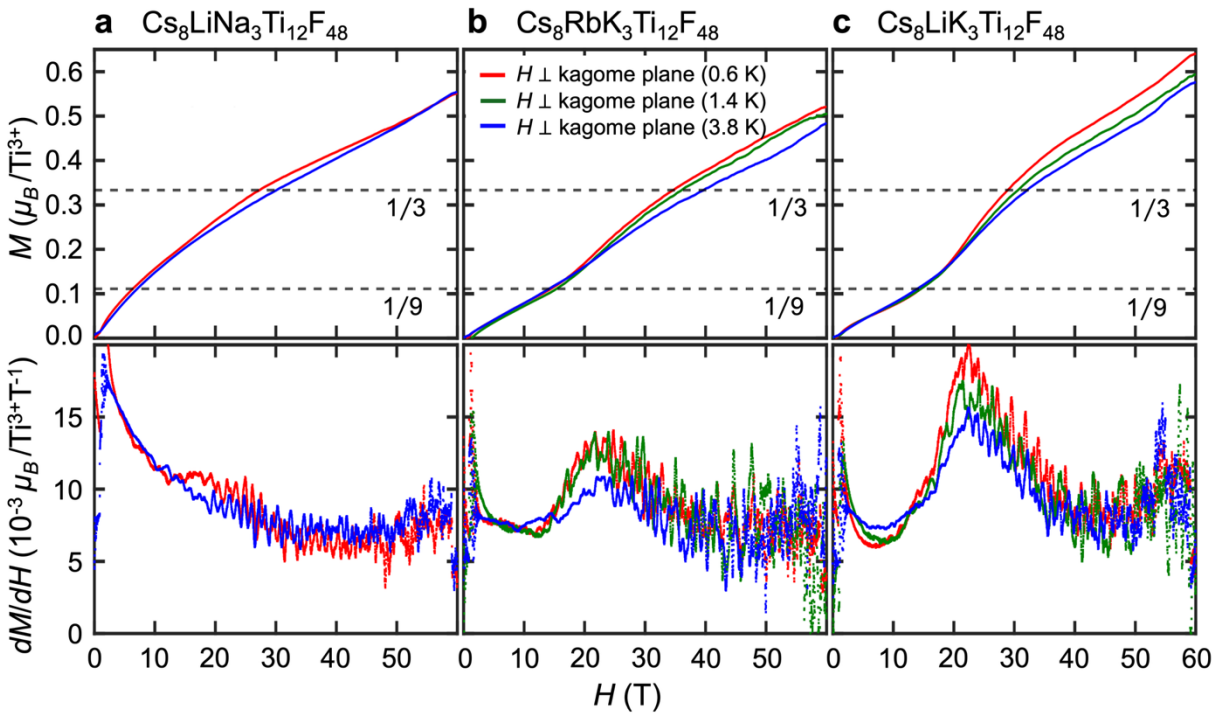

Supplementary Fig. 4 | Temperature dependence of the high-field magnetization. Magnetization of **a**, $Cs_8LiNa_3Ti_{12}F_{48}$, **b,** $Cs_8RbK_3Ti_{12}F_{48}$, and **c**, $Cs_8LiK_3Ti_{12}F_{48}$ measured with the field $H \perp$ kagome plane at 0.6 K (red), 1.4 K (green), and 3.8 K (blue). The dashed horizontal lines indicate the nominal 1/9 and 1/3 fractional magnetization levels. The bottom panels show the corresponding field derivative, dM/dH. No plateau-like feature is observed for LiNa over the entire temperature range. In contrast, the characteristic 1/9 plateau-like features in RbK and LiK broaden with increasing temperature but remain discernible up to 3.8 K.

To evaluate the temperature dependence of the field-induced magnetization features observed at 0.6 K, magnetization measurements were performed up to 3.8 K with $H \perp$ kagome plane. Supplementary Fig. 3 shows the temperature dependence of $M(H)$ and dM/dH for all three compounds. Consistent with the absence of a fractional magnetization plateau, the structurally compressed LiNa compound exhibits a comparatively smooth temperature dependence. Across the measured field range up to 60 T, the magnetization increases monotonically, with the 3.8 K response remaining below the 0.6 K curve owing to thermal suppression of the field-induced magnetization.

The expanded RbK and LiK compounds exhibit a distinctly different temperature evolution. At 0.6 K, the plateau-like field ranges identified in the high-field magnetization data extend from approximately 2.5 to 15.2 T for RbK and from 2.5 to 16.6 T for LiK. With increasing temperature, these intermediate-field features progressively broaden, particularly near their upper-field boundaries. Beyond the plateau-like regime, the magnetization at 0.6 K increases more rapidly than at 1.4 K and 3.8 K, indicating that the crossover out of the plateau-like regime is temperature sensitive.

Correspondingly, the minima in dM/dH become deeper and more sharply defined upon cooling to 0.6 K. Although the features broaden with increasing temperature, the characteristic minima remain discernible up to 3.8 K. These results demonstrate that the 1/9 plateau-like signatures persist up to 3.8 K.

SUPPLEMENTARY NOTE 4: TOPAZ single-crystal neutron diffraction and crystal structure refinement

Single-crystal neutron diffraction data for $Cs_8LiNa_3Ti_{12}F_{48}$, $Cs_8RbK_3Ti_{12}F_{48}$, and $Cs_8LiK_3Ti_{12}F_{48}$ were collected at 300 K using the TOPAZ time-of-flight (TOF) diffractometer at the Spallation Neutron Source [1]. The crystals were mounted on aluminum pins and positioned on the instrument's ambient-temperature goniometer. TOPAZ employs a broad neutron wavelength band of 0.4–3.5 Å and an array of 25 area detectors covering approximately 3.2 sr, enabling efficient three-dimensional mapping of reciprocal space. Data were collected at multiple goniometer orientations to achieve high redundancy and broad reciprocal-space coverage of the Bragg reflections.

The extensive reciprocal-space coverage was particularly important for accurately determining the positions of the F^- ligands surrounding the Ti^{3+} ions, which form the TiF_6 octahedra and define the kagome-related magnetic lattice. Initial data reduction, including peak integration and Lorentz and absorption corrections, was performed using the Mantid software package. The resulting wavelength-resolved integrated intensities were subsequently used for crystallographic refinement.

Structural refinements of the TOPAZ data were performed using JANA2020 [2] against F^2. Here, F denotes the crystallographic structure-factor amplitude, while $F^2 = |F^2|$ is the calculated squared structure-factor amplitude and is directly related to the measured Bragg intensity. The integrated TOPAZ intensities were processed in HKLF 2 format to retain the wavelength information associated with each reflection in the TOF Laue dataset during refinement.

The structural models were refined in the polar monoclinic space group *Cm*. Because the origin is not uniquely defined in this polar space group, one reference atomic position was constrained to prevent origin drift during least-squares refinement. The Li site in the Li-containing compounds and the Rb site in the RbK compound—were therefore fixed at (0, 0, 0).

For the Li-containing compounds, the displacement parameter of Li was weakly constrained by the diffraction data and strongly correlated with other refinement parameters. The Li isotropic displacement parameter, U_{iso}, was therefore fixed at 0.020 $Å^2$ to obtain stable refinement convergence. All remaining atomic positions and displacement parameters were refined freely, with anisotropic displacement parameters used where supported by the data.

The refined atomic coordinates, isotropic displacement parameters (U_{iso}), and site occupancies for the three compounds are summarized in Supplementary Tables 2-4. The alphabetical suffixes a, b, and c identify crystallographically distinct sites generated by the monoclinic distortion from the corresponding parent structural sites. For a two-site splitting, the a site lies on the mirror plane and the b site occupies a general position. For a three-site splitting, the three crystallographically

independent sites are labeled a, b, and c. Unsplit sites on the mirror plane are labeled a. Standard uncertainties are given in parentheses for the last significant digits.

Supplementary Table 2 | Atomic coordinates, Wyckoff site, isotropic displacement parameters (U_{iso}), and site occupancies of $Cs_8LiNa_3Ti_{12}F_{48}$ at 300 K. The structural parameters were obtained from refinement of the TOPAZ single-crystal neutron diffraction data. The numbers in parentheses are standard deviations in the last significant digits.

Atom	Wyckoff site	x	y	z	U_{iso} (Å^2)	Occupancy
Cs1a	2a	0.1506(3)	0.0000	0.6085(4)	0.0266(13)	1
Cs1b	4b	0.39190(14)	0.2499(4)	0.1251(2)	0.0269(8)	1
Cs2a	2a	0.6490(3)	0.0000	0.6060(4)	0.0245(13)	1
Cs3a	2a	0.8967(3)	0.0000	0.3601(4)	0.0333(17)	1
Cs3b	4b	0.63823(14)	0.7502(3)	0.8792(2)	0.0227(6)	1
Cs4a	2a	0.3971(3)	0.0000	0.3597(4)	0.0297(15)	1
Li1a	2a	0.0000	0.0000	0.0000	0.020	1
Na1a	2a	0.5003(3)	0.0000	0.9948(5)	0.0096(11)	1
Na1b	4b	0.28627(15)	0.2503(3)	0.4857(2)	0.0094(6)	1
Ti1a	2a	0.2469(3)	0.0000	0.9684(5)	0.0091(14)	1
Ti1b	4b	0.1435(3)	0.8733(4)	0.2411(4)	0.0097(9)	1
Ti2a	4b	0.53958(18)	0.2493(4)	0.5165(2)	0.0095(7)	1
Ti2b	4b	0.6430(3)	0.8743(4)	0.2409(4)	0.0084(8)	1
Ti2c	4b	0.3931(3)	0.8758(3)	0.7407(4)	0.0083(8)	1
Ti3a	2a	0.7447(3)	0.0000	0.9672(5)	0.0093(15)	1
Ti3b	4b	0.3933(3)	0.6231(4)	0.7394(4)	0.0100(9)	1
F1a	4b	0.70689(19)	0.8993(2)	0.0795(3)	0.0234(8)	1
F1b	4b	0.35095(13)	0.7503(3)	0.7482(2)	0.0248(7)	1
F1c	4b	0.50249(15)	0.3427(2)	0.6413(2)	0.0178(8)	1
F2a	2a	0.1576(3)	0.0000	0.3007(4)	0.0181(10)	1
F2b	4b	0.20483(19)	0.0989(2)	0.0778(3)	0.0271(9)	1
F3a	4b	0.58285(19)	0.3496(2)	0.4057(3)	0.0251(9)	1
F3b	4b	0.62637(14)	0.7497(3)	0.17911(17)	0.0185(5)	1
F3c	4b	0.28405(16)	0.9080(2)	0.8430(3)	0.0211(8)	1
F4a	2a	0.9352(2)	0.0000	0.7359(4)	0.0235(12)	1
F4b	4b	0.78370(17)	0.9067(2)	0.8426(3)	0.0214(8)	1
F5a	2a	0.8563(3)	0.0000	0.0573(4)	0.0269(16)	1
F5b	4b	0.46180(18)	0.6396(2)	0.8940(2)	0.0212(8)	1
F6a	2a	0.4352(3)	0.0000	0.7331(5)	0.0275(14)	1

F6b	4b	0.5808(2)	0.1520(2)	0.4024(2)	0.0251(9)	1
F7a	4b	0.65479(12)	0.2499(3)	0.59160(19)	0.0284(7)	1
F7b	4b	0.7540(2)	0.8483(2)	0.3189(3)	0.0272(10)	1
F7c	4b	0.46183(18)	0.8605(3)	0.8911(2)	0.0217(9)	1
F8a	2a	0.3546(3)	0.0000	0.0574(4)	0.0277(15)	1
F8b	4b	0.25519(16)	0.8480(2)	0.3152(3)	0.0214(8)	1
F9a	2a	0.6558(3)	0.0000	0.3005(3)	0.0203(11)	1
F9b	4b	0.50154(16)	0.84331(19)	0.6381(2)	0.0195(8)	1
F10a	4b	0.52890(18)	0.0985(2)	0.1633(3)	0.0219(8)	1
F10b	4b	0.42735(13)	0.7480(3)	0.42891(19)	0.0269(7)	1
F10c	4b	0.32393(18)	0.1118(2)	0.5894(2)	0.0249(9)	1
F11a	2a	0.6297(3)	0.0000	0.8873(4)	0.0289(16)	1
F11b	4b	0.82420(17)	0.1119(2)	0.5900(2)	0.0251(9)	1
F12a	2a	0.1275(3)	0.0000	0.8872(4)	0.0286(14)	1
F12b	4b	0.52890(18)	0.5968(2)	0.1643(3)	0.0236(9)	1

Supplementary Table 3 | Atomic coordinates, Wyckoff site, isotropic displacement parameters (U_{iso}), and site occupancies of $Cs_8RbK_3Ti_{12}F_{48}$ at 300 K. The structural parameters were obtained from refinement of the TOPAZ single-crystal neutron diffraction data. The numbers in parentheses are standard deviations in the last significant digits.

Atom	Wyckoff site	x	y	z	U_{iso} (Å^2)	Occupancy
Cs1a	2a	0.12230(12)	0.0000	0.6082(3)	0.0229(7)	1
Cs1b	4b	0.37468(13)	0.74041(13)	0.1205(3)	0.0364(6)	1
Cs2a	2a	0.63771(18)	0.0000	0.6067(4)	0.0367(10)	1
Cs3a	2a	0.88734(12)	0.0000	0.3724(3)	0.0363(9)	1
Cs3b	4b	0.64338(13)	0.75150(13)	0.8713(2)	0.0315(6)	1
Cs4a	2a	0.39534(19)	0.0000	0.3734(4)	0.0336(9)	1
Rb1a	2a	0.0000	0.0000	0.0000	0.0727(11)	1
Ti1a	2a	0.2528(2)	0.0000	0.9922(3)	0.0123(7)	1
Ti1b	4b	0.14542(17)	0.12623(15)	0.2537(3)	0.0143(6)	1
Ti2a	4b	0.51227(15)	0.74876(14)	0.4992(3)	0.0087(4)	1
Ti2b	4b	0.62171(14)	0.12661(13)	0.2311(3)	0.0180(6)	1
Ti2c	4b	0.37354(15)	0.12353(13)	0.7313(3)	0.0162(6)	1
Ti3a	2a	0.7541(2)	0.0000	0.9925(4)	0.0153(7)	1
Ti3b	4b	0.39428(16)	0.37634(15)	0.7560(3)	0.0139(6)	1

K1a	2a	0.49852(15)	0.0000	0.9786(3)	0.0113(6)	1
K1b	4b	0.26496(12)	0.74304(8)	0.5008(2)	0.0107(4)	1
F1a	4b	0.34346(17)	0.25214(11)	0.7659(3)	0.0520(9)	1
F1b	4b	0.48414(10)	0.65873(9)	0.62872(19)	0.0264(5)	1
F1c	4b	0.6943(2)	0.90748(12)	0.0832(3)	0.0846(11)	1
F2a	2a	0.14327(19)	0.0000	0.3162(3)	0.0298(7)	1
F2b	4b	0.18441(17)	0.90964(13)	0.0844(2)	0.0405(6)	1
F3a	4b	0.59831(9)	0.66255(9)	0.42323(17)	0.0194(4)	1
F3b	4b	0.6552(2)	0.25074(11)	0.1995(3)	0.0667(10)	1
F3c	4b	0.31120(17)	0.09528(13)	0.8900(3)	0.0608(8)	1
F4a	2a	0.93906(15)	0.0000	0.7460(3)	0.0196(6)	1
F4b	4b	0.8039(2)	0.09255(17)	0.8838(4)	0.0782(11)	1
F5a	2a	0.8482(2)	0.0000	0.0927(4)	0.137(3)	1
F5b	4b	0.47151(15)	0.35067(11)	0.88589(19)	0.0321(5)	1
F6a	2a	0.40952(14)	0.0000	0.7056(3)	0.0276(7)	1
F6b	4b	0.54406(13)	0.84336(11)	0.3734(2)	0.0299(5)	1
F7a	4b	0.60795(10)	0.79116(12)	0.59939(19)	0.0241(4)	1
F7b	4b	0.72031(15)	0.11305(16)	0.3429(4)	0.0865(14)	1
F7c	4b	0.48172(15)	0.13737(16)	0.8179(3)	0.0464(7)	1
F8a	2a	0.3440(2)	0.0000	0.1032(4)	0.084(2)	1
F8b	4b	0.25889(11)	0.13467(16)	0.3191(3)	0.0546(9)	1
F9a	2a	0.58733(14)	0.0000	0.2562(3)	0.0276(6)	1
F9b	4b	0.43055(11)	0.16202(10)	0.57347(19)	0.0221(4)	1
F10a	4b	0.51284(16)	0.86874(19)	0.1420(4)	0.0831(13)	1
F10b	4b	0.42191(10)	0.29136(11)	0.39828(19)	0.0253(4)	1
F10c	4b	0.26737(13)	0.88250(16)	0.6531(3)	0.0424(6)	1
F11a	2a	0.6560(2)	0.0000	0.8881(3)	0.125(3)	1
F11b	4b	0.81251(12)	0.89879(13)	0.6274(3)	0.0369(6)	1
F12a	2a	0.1544(2)	0.0000	0.8705(3)	0.091(2)	1
F12b	4b	0.52763(14)	0.61312(17)	0.1927(2)	0.0458(7)	1

Supplementary Table 4 | Atomic coordinates, Wyckoff site, isotropic displacement parameters (U_{iso}), and site occupancies of $Cs_8LiK_3Ti_{12}F_{48}$ at 300 K. The structural parameters were obtained from refinement of the TOPAZ single-crystal neutron diffraction data. The numbers in parentheses are standard deviations in the last significant digits.

Atom	Wyckoff site	x	y	z	U_{iso} (Å^2)	Occupancy

Cs1a	2a	0.1114(7)	0.0000	0.6194(12)	0.034(4)	1
Cs1b	4b	0.8596(3)	0.2491(7)	0.1032(4)	0.0294(13)	1
Cs2a	2a	0.6105(7)	0.0000	0.6178(12)	0.029(3)	1
Cs3a	2a	0.8700(7)	0.0000	0.3876(9)	0.027(3)	1
Cs3b	4b	0.6178(3)	0.2509(8)	0.8678(5)	0.0352(16)	1
Cs4a	2a	0.3671(6)	0.0000	0.3846(11)	0.030(3)	1
Ti1a	2a	0.2632(6)	0.0000	1.0115(11)	0.013(3)	1
Ti1b	4b	0.1166(6)	0.1239(7)	0.2429(10)	0.015(2)	1
Ti2a	4b	0.9745(3)	0.2493(7)	0.4753(5)	0.0124(12)	1
Ti2b	4b	0.6182(6)	0.1243(7)	0.2434(9)	0.0116(18)	1
Ti2c	4b	0.3680(6)	0.1249(7)	0.7440(9)	0.0113(19)	1
Ti3a	2a	0.7599(6)	0.0000	1.0098(10)	0.012(3)	1
Ti3b	4b	0.3661(6)	0.3753(7)	0.7414(10)	0.015(2)	1
Li1a	2a	0.0000	0.0000	0.0000	0.020	1
K1a	2a	0.5018(5)	0.0000	0.9906(8)	0.0079(19)	1
K1b	4b	0.2303(3)	0.2489(6)	0.4940(4)	0.0094(10)	1
F1a	2a	0.8596(6)	0.0000	0.1177(10)	0.047(4)	1
F1b	4b	0.4861(4)	0.3931(4)	0.7938(6)	0.0267(17)	1
F2a	2a	0.5759(5)	0.0000	0.2470(9)	0.022(2)	1
F2b	4b	0.4144(5)	0.1569(4)	0.5761(6)	0.0413(18)	1
F3a	4b	0.9070(3)	0.1580(4)	0.5675(6)	0.0264(14)	1
F3b	4b	0.7101(5)	0.0970(6)	0.1151(8)	0.042(3)	1
F3c	4b	0.3707(3)	0.2497(5)	0.8005(3)	0.0291(11)	1
F4a	2a	0.8585(5)	0.0000	0.6814(8)	0.024(2)	1
F4b	4b	0.8254(5)	0.0932(5)	0.9119(7)	0.031(2)	1
F5a	4b	0.5270(5)	0.3448(5)	0.3707(9)	0.043(2)	1
F5b	4b	0.8240(5)	0.4057(4)	0.9113(7)	0.030(2)	1
F5c	4b	0.1614(2)	0.2497(5)	0.2394(4)	0.0208(10)	1
F6a	4b	0.8784(3)	0.2562(8)	0.3661(4)	0.057(2)	1
F6b	4b	0.5340(4)	0.1484(4)	0.1168(7)	0.0391(19)	1
F6c	4b	0.2535(4)	0.1414(5)	0.6839(7)	0.0358(19)	1
F7a	4b	0.0715(3)	0.2443(8)	0.5827(5)	0.050(2)	1
F7b	4b	0.6992(6)	0.1021(4)	0.3717(7)	0.036(2)	1
F7c	4b	0.4864(4)	0.1080(5)	0.7975(7)	0.0292(19)	1
F8a	2a	0.0714(6)	0.0000	0.2438(9)	0.021(2)	1
F8b	4b	0.7079(4)	0.4050(5)	0.1141(8)	0.037(2)	1
F9a	2a	0.3621(6)	0.0000	0.6833(8)	0.026(2)	1
F9b	4b	0.0331(5)	0.3455(4)	0.3773(7)	0.045(2)	1
F10a	2a	0.1679(6)	0.0000	0.9019(11)	0.054(4)	1
F10b	4b	0.0353(4)	0.1496(5)	0.1090(7)	0.0341(18)	1

F11a	2a	0.3626(5)	0.0000	0.1194(10)	0.043(3)	1
F11b	4b	0.1944(5)	0.1020(5)	0.3707(7)	0.0325(17)	1
F12a	2a	0.6672(7)	0.0000	0.8983(10)	0.047(4)	1
F12b	4b	0.2502(4)	0.3579(5)	0.6873(7)	0.036(2)	1

SUPPLEMENTARY NOTE 5: FONDER neutron diffraction and joint neutron and X-ray structural refinement

To obtain an independent and more highly constrained structural models of $Cs_8RbK_3Ti_{12}F_{48}$, and additional single-crystal neutron diffraction experiment was performed at room temperature using the FONDER four-axis diffractometer at the JRR-3 research reactor of the Japan Atomic Energy Agency[3]. A monochromatic neutron beam with a wavelength of 1.2476 Å was used. Bragg reflections were measured using standard ω-step scans, providing high-resolution diffraction intensities for detailed structural refinement.

The FONDER neutron diffraction data were jointly refined with room-temperature single-crystat X-ray diffraction data collected using a DIP3200 X-ray diffractometer (Bruker AXS) with a Mo target. The X-ray measurements employed Mo *Kα* radiation with $\lambda = 0.71073$ Å. The joint neutron and X-ray refinement was performed using JANA2020 [2], taking advantage of the complementary scattering contrasts of the two diffraction techniques. The X-ray dataset provides strong constraints on the positions and displacement parameters of the heavier Cs, Rb, K, and Ti atoms, whereas the neutron data provide complementary sensitivity to the F sublattice.

The FONDER neutron and X-ray datasets were jointly refined in the monoclinic space group *Cm* (No. 8). For the FONDER neutron dataset, the measured reflections were represented by structure-factor amplitudes *F* and their standard uncertainties, *dF,* and the refinement was performed against *F*. Dataset-specific weighting factors were applied to balance the contributions of the neutron and X-ray data in the joint least-squares refinement. Absorption and extinction corrections were applied separately to each dataset before the joint refinement. The resulting atomic coordinates define the structural model used to construct the polyhedral representation and the isolated Ti-F framework shown in main-text Figs. 1d and 1e, respectively.

Comparison of the TOPAZ and FONDER/X-ray structural models.

To assess the reproducibility of the structural determination, the structure obtained independently from the 300 K TOPAZ neutron diffraction data was compared with that obtained from the joint FONDER neutron/X-ray refinement.

Both refinements yield the same monoclinic *Cm* space group and the same overall atomic arrangement. The lattice parameters are closely comparable [Supplementary Table 5]. The TOPAZ refinement gives $a = 15.151(3)$ Å, $b = 15.238(3)$ Å, $c = 10.837(4)$ Å, and $\beta = 90.44(2)°$, whereas the FONDER/X-ray refinement gives $a = 15.169(12)$ Å, $b = 15.304(12)$ Å, $c = 10.759(10)$ Å, and $\beta = 90.57(8)°$ The corresponding unit-cell volumes are 2501.9(1) and 2497.5(5) Å, respectively, differing by only approximately 0.18%.

The refined Cs, Rb, K, and Ti sublattices are in good overall agreement between the two structural models, although larger site-dependent differences are observed for some individual F coordinates and displacement parameters. Thus, the independently obtained TOPAZ and FONDER/X-ray refinements provide consistent descriptions of the same *Cm* crystal structure, supporting the robustness of the symmetry assignment and the principal structural features while allowing for modest quantitative differences in some local structural parameters.

Supplementary Table 5 | Comparison of room-temperature crystallographic parameters of $Cs_8RbK_3Ti_{12}F_{48}$ obtained from the FONDER/X-ray and TOPAZ refinements. The FONDER-based structural parameters were obtained from the joint refinement of FONDER single-crystal neutron diffraction and single-crystal X-ray diffraction data, whereas the TOPAZ parameters were obtained independently from TOPAZ single-crystal neutron diffraction data. The relative difference is defined as $|X_{\mathrm{FONDER}} - X_{\mathrm{TOPAZ}}|/X_{\mathrm{TOPAZ}} \times 100\%$. Standard uncertainties are given in parentheses for the last significant digits.

300K	FONDER-based refinement	TOPAZ-based refinement	Relative difference
Space group	*Cm*	*Cm*	-
a (Å)	15.169(12)	15.151(3)	0.12%
b (Å)	15.304(12)	15.238(3)	0.43%
c (Å)	10.759(10)	10.837(4)	0.72%
α (°)	90.0	90.0	-
β (°)	90.57(8)	90.44(2)	0.14%
γ (°)	90.0	90.0	-
V (Å^3)	2497.5(4)	2501.9(1)	0.17%
Z	2	2	-

Supplementary Table 6 | Atomic coordinates, Wyckoff sites, isotropic displacement parameters (U_{iso}), and site occupancies of $Cs_8RbK_3Ti_{12}F_{48}$, obtained from joint refinement of the FONDER single-crystal neutron diffraction and X-ray diffraction data. The same atomic-site labeling convention used in Supplementary Tables 2-4 is followed. Standard uncertainties are given in parentheses for the last significant digits.

Atom	Wyckoff site	x	y	z	U_{iso} (Å^2)	Occupancy
Cs1a	2a	0.12963(6)	0.000000	0.60490(8)	0.033193(3)	1.0
Cs1b	4b	0.38074(4)	0.75005(6)	0.12271(5)	0.034706(5)	1.0
Cs2a	2a	0.62956(6)	0.000000	0.60514(8)	0.032893(3)	1.0
Cs3a	2a	0.88605(6)	0.000000	0.37133(9)	0.034390(3)	1.0
Cs3b	4b	0.63794(4)	0.75001(5)	0.88904(5)	0.029771(18)	1.0
Cs4a	2a	0.38632(6)	0.000000	0.37149(9)	0.034724(3)	1.0
Rb1a	2a	0.00000	0.000000	0.00000	0.160710(17)	1.0
Ti1a	2a	0.23861(12)	0.000000	0.9776(2)	0.011328(4)	1.0
Ti1b	4b	0.13410(13)	0.12503(12)	0.2471(2)	0.012577(3)	1.0
Ti2a	4b	0.52707(11)	0.75002(6)	0.51424(14)	0.013241(3)	1.0
Ti2b	4b	0.63364(13)	0.12491(12)	0.2465(2)	0.011474(3)	1.0
Ti2c	4b	0.38316(13)	0.12530(12)	0.7462(2)	0.012374(3)	1.0
Ti3a	2a	0.73829(12)	0.000000	0.9770(2)	0.012071(4)	1.0
Ti3b	4b	0.38288(13)	0.37463(12)	0.7468(2)	0.011746(3)	1.0
K1a	2a	0.4983(2)	0.000000	0.9990(4)	0.008566(3)	1.0
K1b	4b	0.27181(11)	0.75003(7)	0.49351(17)	0.009225(3)	1.0
F1a	4b	0.3364(4)	0.2499(2)	0.7462(5)	0.021503(12)	1.0
F1b	4b	0.4694(4)	0.6555(4)	0.6119(5)	0.039751(15)	1.0
F1c	4b	0.6759(4)	0.9071(4)	0.0749(5)	0.037864(17)	1.0
F2a	2a	0.1411(5)	0.000000	0.3066(7)	0.025962(18)	1.0
F2b	4b	0.1789(4)	0.9064(4)	0.0780(4)	0.033537(15)	1.0
F3a	4b	0.5940(4)	0.6572(4)	0.4190(4)	0.025935(12)	1.0
F3b	4b	0.6277(5)	0.2498(2)	0.1880(5)	0.029503(16)	1.0
F3c	4b	0.2917(4)	0.0954(4)	0.8731(7)	0.041758(18)	1.0
F4a	2a	0.9236(4)	0.000000	0.7416(7)	0.023656(16)	1.0
F4b	4b	0.7881(4)	0.0956(4)	0.8689(7)	0.041804(16)	1.0
F5a	2a	0.8316(5)	0.000000	0.0845(7)	0.049021(3)	1.0
F5b	4b	0.4652(4)	0.3494(4)	0.8713(7)	0.038836(15)	1.0

F6a	2a	0.4244(4)	0.000000	0.7412(7)	0.023669(17)	1.0
F6b	4b	0.5935(4)	0.8437(4)	0.4190(4)	0.027253(12)	1.0
F7a	4b	0.6232(4)	0.7507(4)	0.6182(5)	0.050596(2)	1.0
F7b	4b	0.7502(4)	0.1436(4)	0.2972(5)	0.031276(13)	1.0
F7c	4b	0.4666(4)	0.1477(4)	0.8713(7)	0.037476(15)	1.0
F8a	2a	0.3339(5)	0.000000	0.0853(7)	0.046055(3)	1.0
F8b	4b	0.2503(4)	0.1435(4)	0.2962(5)	0.031282(13)	1.0
F9a	2a	0.6404(5)	0.0000	0.3064(7)	0.027309(19)	1.0
F9b	4b	0.4705(4)	0.1542(4)	0.6124(5)	0.036017(14)	1.0
F10a	4b	0.5154(4)	0.8925(4)	0.1910(5)	0.030766(13)	1.0
F10b	4b	0.4318(4)	0.2491(4)	0.4020(7)	0.047688(2)	1.0
F10c	4b	0.3047(4)	0.8984(4)	0.6126(5)	0.029995(12)	1.0
F11a	2a	0.6387(5)	0.000000	0.8631(7)	0.043021(2)	1.0
F11b	4b	0.8040(4)	0.8984(4)	0.6132(5)	0.031427(13)	1.0
F12a	2a	0.1401(5)	0.000000	0.8613(7)	0.047302(3)	1.0
F12b	4b	0.5155(4)	0.6101(4)	0.1919(5)	0.032103(14)	1.0

SUPPLEMENTARY NOTE 6: DFT-derived magnetic exchange parameters.

Supplementary Table 7 | DFT-derived nearest-neighbor exchange interactions in the $Cs_8AB_3Ti_{12}F_{48}$ family. Exchange pathways and Heisenberg couplings for $Cs_8LiNa_3Ti_{12}F_{48}$ (LiNa), $Cs_8RbK_3Ti_{12}F_{48}$ (RbK), and $Cs_8LiK_3Ti_{12}F_{48}$ (LiK), as determined from DFT-based energy mapping using the selected U values shown in Fig. 4. The normalized exchange constants, J_i/J_{max}, are given relative to the strongest nearest-neighbor interaction in each compound. Under the Hamiltonian convention $H = \sum_{i<j} J_{ij}\mathbf{S}_i.\mathbf{S}_j$, positive and negative J_{ij} denote antiferromagnetic and ferromagnetic interactions, respectively. The assignments identify exchange pathways belonging to the A and B subsystems and the corresponding zigzag connections defined in main-text Fig. 4a.

Exchange interaction	LiNa		RbK		LiK		Assignment
	J_i (K)	J_i/J_{max}	J_i (K)	J_i/J_{max}	J_i (K)	J_i/J_{max}	
$J_{2c\text{-}3b}$	29.6	0.368	46.8	0.472	38.4	0.513	Chain-A
$J_{2c\text{-}2c}$	75.3	0.936	89.1	0.899	22.0	0.294	Chain-A
$J_{3b\text{-}3b}$	74.7	0.928	99.1	1.000	32.2	0.430	Chain-A
$J_{1b\text{-}2b}$	80.5	1.000	41.5	0.419	45.1	0.602	Chain-B
$J_{1b\text{-}1b}$	59.7	0.742	36.2	0.365	51.7	0.692	Chain-B
$J_{2b\text{-}2b}$	60.2	0.748	34.3	0.346	74.8	1.000	Chain-B
$J_{1a\text{-}2c}$	40.5	0.503	41.2	0.415	42.8	0.572	Chain-A-zigzag
$J_{2a\text{-}2c}$	60.2	0.749	33.0	0.333	46.8	0.626	Chain-A-zigzag
$J_{2a\text{-}3b}$	52.8	0.656	51.9	0.524	45.0	0.602	Chain-A-zigzag
$J_{3a\text{-}3b}$	37.7	0.469	26.9	0.272	46.2	0.618	Chain-A-zigzag
$J_{1a\text{-}1b}$	7.9	0.098	53.9	0.544	29.3	0.392	Chain-B-zigzag
$J_{1b\text{-}2a}$	-6.3	-0.078	53.2	0.537	50.9	0.680	Chain-B-zigzag
$J_{2a\text{-}2b}$	9.9	0.123	38.3	0.387	40.8	0.546	Chain-B-zigzag
$J_{2b\text{-}3a}$	-5.1	-0.064	52.2	0.527	7.87	0.105	Chain-B-zigzag

SUPPLEMENTARY NOTE 7: Temperature dependence of high-field magnetization in powder samples.

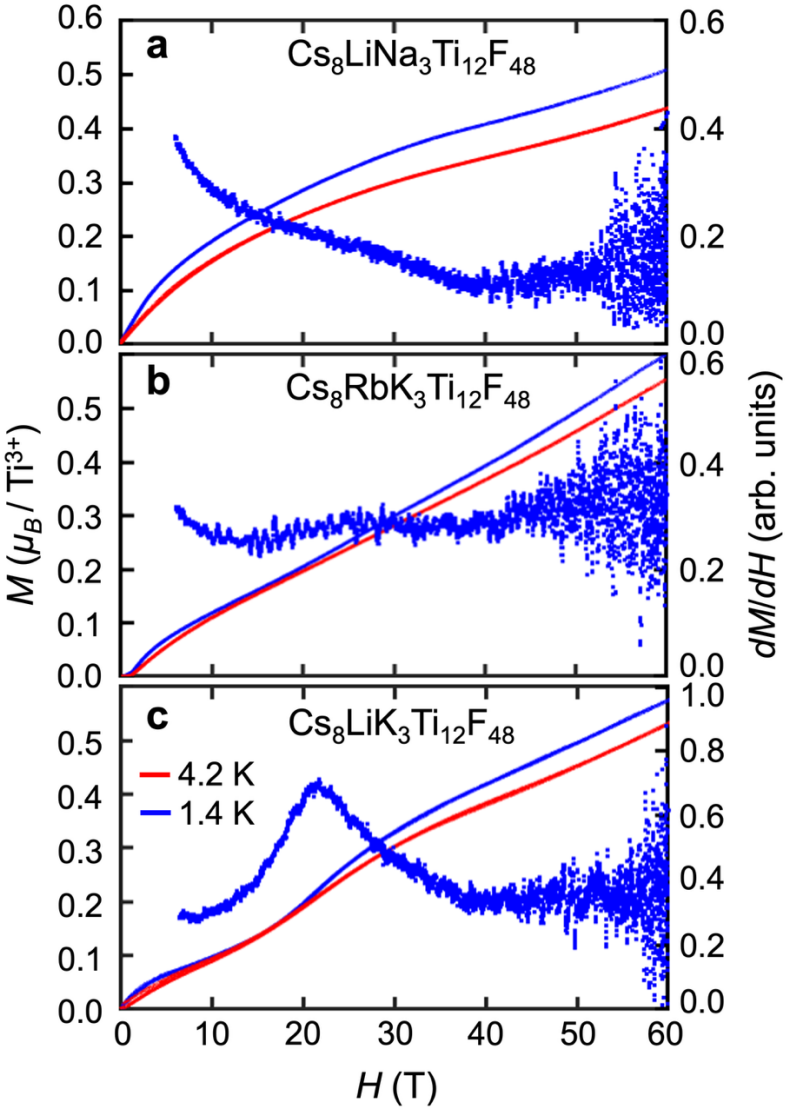

Supplementary Fig. 5 | Temperature dependence of high-field magnetization in powder samples of the $Cs_8AB_3Ti_{12}F_{48}$ family. Field-dependent magnetization, $M(H)$ (left y-axis), and the corresponding field derivative, dM/dH (right y-axis) measured in pulsed magnetic fields up to 60 T for **a,** $Cs_8LiNa_3Ti_{12}F_{48}$ **b,** $Cs_8RbK_3Ti_{12}F_{48}$ and **c,** $Cs_8LiK_3Ti_{12}F_{48}$. Magnetization data collected at 4.2 K and 1.4 K are shown by the red and blue solid lines, respectively, while the blue points show dM/dH at 1.4 K. The RbK and LiK compounds exhibit pronounced field-dependent features in dM/dH within the intermediate-field regime, whereas the LiNa compound shows a comparatively smooth field dependence. Measurements were performed on powder samples at the International MegaGauss Science Laboratory, Institute for Solid State Physics, University of Tokyo.

REFERENCES

1. Coates, L. et al. A suite-level review of the neutron single-crystal diffraction instruments at Oak Ridge National Laboratory. *Rev. Sci. Instrum.* **89**, 092802 (2018).

2. Petříček, V., Palatinus, L., Plášil, J. & Dušek, M. Jana2020 – a new version of the crystallographic computing system Jana. *Z. Kristallogr. - Cryst. Mater.* **238**, 271-282 (2023).

3. Takahashi, M. et al. Four-circle neutron diffractometer FONDER at JRR-3: Quantitative reciprocal-space measurements in structural physics. *J. Phys. Soc. Jpn.* **93**, 091006 (2024).